Neural Computing and Applications manuscript No.
(will be inserted by the editor)

Simultaneous Segmentation of the Optic Disc and Fovea in Retinal Images using Evolutionary Algorithms

Enrique J. Carmona* · **José M. Molina-Casado**

Received: date / Accepted: date

Abstract In this work, we present a new methodology to simultaneously segment anatomical structures in medical images. Additionally, this methodology is instantiated in a method that is used to simultaneously segment the optic disc (OD) and fovea in retinal images. The OD and fovea are important anatomical structures that must be previously identified in any image based computer aided diagnosis system dedicated to diagnosing retinal pathologies that cause vision problems. Basically, the simultaneous segmentation method uses an OD-fovea model and an evolutionary algorithm. On the one hand, the model is built using the intra-structure relational knowledge, associated with each structure, and the inter-structure relational knowledge existing between both and other retinal structures. On the other hand, the evolutionary algorithm (differential evolution) allows us to automatically adjust the instance parameters that best approximate the OD-fovea model in a given retinal image. The method is evaluated in the MESSIDOR public database. Compared with other recent segmentation methods in the related literature, competitive segmentation results are achieved. In particular, a sensitivity and specificity of 0.9072 and 0.9995 are respectively obtained for the OD. Considering a success when the distance between the detected and actual center is less than or equal to η times the OD radius, the success rates obtained for the fovea are 97.3% and 99.0% for $\eta = 1/2$ and $\eta = 1$, respectively. The segmentation average time per image is 29.35 s.

Keywords Evolutionary algorithm · Differential evolution · Optic disc · Fovea · Segmentation · Retinal image

Enrique J. Carmona (*Corresponding author)
E-mail: ecarmona@dia.uned.es
José M. Molina-Casado
E-mail: jmolina_79@hotmail.com

Department of Artificial Intelligence, Escuela Técnica Superior de Ingeniería Informática, Universidad Nacional de Educación a Distancia, Madrid, Spain

1 Introduction

One of the first requirements of any image based computer aided diagnosis system is the previous identification of the main anatomical structures associated with the pathology to be diagnosed. In particular, the first step for automatic screening of most retinal pathologies is localization and segmentation of the optic disc (OD) and fovea/macula (see Fig. 1). For example, OD segmentation is an important step for the detection of glaucoma. The localization of an anatomical structure can also facilitate the automatic detection of other anatomical structures. For example, OD localization has been used traditionally as a reference to detect the fovea. Additionally, in order to detect signs of several retinal diseases, the localization of the different anatomical structures can also be used as landmarks. For example, previous OD localization is necessary for the computation of some important diagnostic indexes for hypertensive/sclerotic retinopathy based on vasculature [1]. In the same way, the proximity of a bright or dark lesion to the fovea can indicate a high risk of maculopathy. In particular, the risk of macular edema can be evaluated by computing the distance of exudates to the fovea center. Finally, it is important to know the localization of the anatomical structures to avoid confusing them with other pathological structures. For example, the OD may be easily confounded with large exudative

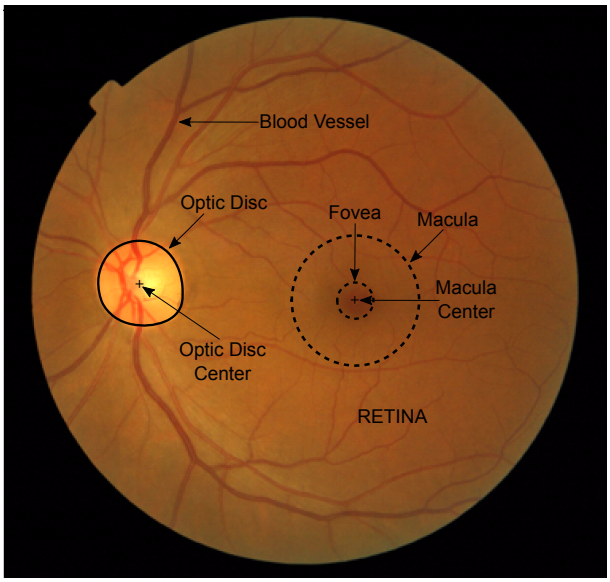

Fig. 1: Main anatomical structures in a retinal image (left eye).

lesions [2, 3, 4], and the fovea, with retinal hemorrhages or microaneurysms [5, 6].

The OD segmentation task goal is usually to obtain its contour. On the other way, as the fovea contour is not sharply defined, the fovea segmentation task goal is usually to obtain its center as accurately as possible. Many strategies have been used to segment the OD and fovea. In a first classification, the different approaches can be divided into two groups: (i) one that just uses the intrinsic properties of each anatomical structure (brightness, darkness, shape, etc.) in order to segment it; and (ii) another that, additionally, also uses geometrical properties between both structures and other structures such as, for example, the vascular tree. Henceforth, following the same nomenclature as that used in [7], the first type of knowledge will be denoted as *intra-structure relational knowledge* (intra-SRK) and, the second one, as *inter-structure relational knowledge* (inter-SRK).

Regarding those approaches that just use intra-SRK to segment the OD, most of them apply a previous step to search for a reference point that is an approximate position of the OD center or, alternatively, any other point that is contained inside the OD. The idea is to limit OD segmentation to a sub-region of the original image, big enough to contain the OD and centered at the reference point. In this context, and taking into account the most recent works, the segmentation stage has been tackled with different methods, for example, mathematical morphology [8, 9, 10], Hough transform [8, 11], watershed transformation [10], meta-heuristics [12, 13, 14, 15], active contours [16], topological active nets [13], fitting of incrementally complex contour models at increasing resolutions [17], sliding band filters [18], level set models [19], and super-pixel classification [20]. Alternatively, the solutions proposed in the literature to locate fovea using just intra-SRK are scarce [21]. Most fovea segmentation approaches have used information from other previously segmented or detected retinal structures, such as the OD or vascular tree.

Regarding those approaches that use intra- and inter-SRK to segment one or more structures, most of them perform the segmentation sequentially. For example, structure-1 segmentation is based on structure-1 intra-SRK and previous structure-2 segmentation (use of inter-SRK). In turn, structure-2 segmentation is based on structure-2 intra-SRK and previous structure-3 segmentation (use of inter-SRK) and, finally, structure-3 segmentation is done through the single use of structure-3 intra-SRK. In this context, OD segmentation is normally made using the vascular tree (previously segmented) as a reference [9, 22, 23]. Note that the junction point of the superior and inferior arcades of the vascular tree is very close to the OD center. On the other way, localization of the fovea is obtained using the position of the OD as a reference [24] and, in other cases, additionally [25, 26, 27] or alternatively [28], the vascular tree. The inter-SRK used in these cases makes use of two properties: (i) the fovea center is located on average at 5 OD radii from the OD center following the axis of symmetry separating the superior and inferior arcades; and (ii) the fovea is always included in the region covered by the two arcades.

There are some works in the literature that simultaneously use both types of knowledge and they are fairly recent. Thus, in [29], each retinal image is processed to compute several maps highlighting the different anatomical structures (vessels, fovea and OD). Then, fovea and OD center candidates are found using seed detectors in the respective maps. After selecting a set of macula/OD pairs, the best candidates are sent to the OD segmentation method based on local K-means followed by a polynomial fitting regularization step. Pair scores are updated and the final best macula/OD center pair is chosen, including the OD contour. In [30], the authors developed and trained a convolutional neural network to automatically and simultaneously segment the OD, fovea and blood vessels; their results are competitive but the main inconvenience is the high computational cost necessary to train and use the neural network.

All the bibliographic references mentioned above are just a representative sample of the substantial amount of approaches reported in the literature. However, seg-

mentation of anatomical structures in retinal images remains an open problem today and new approaches continue to appear in this area. Current trends are directed towards the joint use of intra- and inter-SRK, but considering two types of segmentation strategies: sequential and simultaneous. The main drawback of sequential segmentation is that a failure in segmentation or detection of the first structure (usually the OD) will likely result in a segmentation failure of the second structure (usually the fovea) [26]. In other cases, there are methods that propose to automatically segment a structure, assuming that the segmentation of other structure is already known. However, the success of this kind of methods will always be conditioned to the degree of success of the assumption made. That is why in this work we propose a new methodology aimed at the simultaneous segmentation of two or more structures, taking advantage of all available relational knowledge (intra- and inter-SRK) from the structures to be segmented in the process. In addition, this methodology will be applied to the simultaneous segmentation of the disc and fovea in fundus images, considering the following steps: (1) creation of an OD model based on OD intra-SRK; (2) creation of a fovea model based on fovea intra-SRK; (3) creation of an OD-fovea model based on combining the two intra-SRK models and the existing inter-SRK between both structures; this model will be used as a reference in order to search for the best OD-fovea instance that minimizes error with respect to said model in a given retinal image; and (4) an evolutionary algorithm will be proposed as a new segmentation method to solve this minimization problem.

The rest of the paper is organized as follows. Section 2 describes the retinal image database used in this work. Section 3 provides an explanation of the proposed methodology, and Section 4 shows the necessary steps to instantiate it in a simultaneous segmentation method of OD and fovea. Section 5 presents the segmentation results obtained and their discussion. Finally, the conclusions are provided in Section 6.

2 Materials

We have used three different databases for the experiments: MESSIDOR [31, 32], ONHSD [16, 33], and DIARETDB1 [34, 35]. The MESSIDOR database contains 1200 retinal images, RGB format, 8 bits/pixel, $FOV = 45^o$ and three different sizes: 1440×960, 2240×1488 and 2304×1536. The OD ground truth for this database is available on the MESSIDOR web [31]. The annotations of fovea centers from 1136 MESSIDOR images were created and published by the University of Huelva [36]. The remaining 64 annotations, up to 1200, were kindly provided by the authors of [25]. The ONHSD database contains 99 retinal images, RGB format, 8 bits/pixel, $FOV = 45^o$ and size of 640×480. Here, only the optic disc ground truth is provided on the web of this database [33]. Specifically, each OD contour used as a reference was obtained as a result of averaging four OD contours traced by four different experts. Finally, the DIARETDB1 database contains 89 retinal images, RGB format, $FOV = 50^o$ and size of 1500×1152. On the web of this database [34], there is no ground truth for the fovea and OD. Here, the fovea annotations were obtained from [27]. All the mentioned databases contain healthy eyes and eyes with several kinds of retinopathies. A more detailed description for each database can be consulted in their respective bibliographic references.

3 Methodology

A block diagram, which describes the generic methodology proposed for simultaneously segmenting two anatomical structures in medical images, is shown in figure 2. It should be noted that the methodology consists of two stages. In the first, the model is learned and, in the second, the learned model is used to simultaneously segment two anatomical structures. On the one hand, the learning of the model consists of the following steps. First, making use of the intra-SRK associated with structure #1, a model of such a structure is generated, called the *intra-SRK model*. The process is repeated for structure #2. In both cases, a medical image database, where the ground truth of each structure is known, should be used. Next, the two intra-SRK models are combined into a new model, named the *intra&inter-SRK model*, which also incorporates the inter-SRK associated with both structures. On the other hand, the stage related to the use of the model involves transforming the problem of simultaneously segmenting the structure #1 and #2 in a medical image into a new optimization problem consisting of finding an anatomical structure instance that minimizes its error with respect to the learned intra&inter-SRK model. Owing to the high number of model parameters and their real definition domain, a brute force method can not be used to obtain the optimal instance. Therefore, an evolutionary algorithm is proposed in order to find an optimal (or near optimal) solution. In this way, the best individual of the population obtained at the end of the evolutionary process will represent the searched-for solution. Note that there is a preprocessing step that is applied in both stages. It works in the same way in both cases and its main purpose is to ensure that the learning of the

model and the segmentation process are independent of the size of the input image.

The presented methodology could be extended recursively in two directions. For example, on the one hand, the two structure intra&inter-SRK model could be combined with the intra-SRK model of a third structure, including the inter-SRK between the three structures, in order to create a new intra&inter-SRK model. On the other hand, three intra-SRK models, together with the corresponding inter-SRK, could be combined to create a new intra&inter-SRK model. In both cases, the new intra&inter-SRK model would allow us to simultaneously segment three structures, and so on.

4 OD and fovea simultaneous segmentation

This section describes the steps followed to instantiate the methodology previously described into a new method to simultaneously segment the OD and fovea in retinal images. First, an image preprocessing step will be detailed. Second, the steps to build the OD and fovea models (intra-SRK models) will be described. Third, the combination of both intra-SRK models and the injection of existing relational knowledge between OD and fovea will allow us to define the OD-fovea model (intra&inter-SRK model). Finally, we will describe how the OD-fovea model will be used by a segmentation method based on an evolutionary algorithm that will allow us to find the best approximation for the OD and fovea in a given retina image.

4.1 Preprocessing

Here we describe a set of image preprocessing steps that will be applied both to the generation of the different models and the evaluation of their respective instances. They are the following: (a) reduction of input image size to obtain a common work resolution independent of the original image resolution; (b) image horizontal flipping if the type of eye does not match with that established by default (left); and (c) normalization of the three RGB channels.

The reduction of size is done using a scale factor oriented to obtain a fixed image resolution value. This reduction has several advantages. First, it helps to decrease the image processing time and also eliminates some noisy artifacts that are present in the original image. Second, the use of a fixed resolution will allow us to implement and configure models and segmentation methods that are independent of the original size and resolution of the input image. Thus, assuming that we will work with a standard resolution K_0, defined by the user and expressed in $pixel/mm$, Eq. (1) establishes the scale factor α needed to transform the input image to the resolution chosen [7], where $A^{\theta}_{mm^2}$ and A_{px} represent the input image retinal area, expressed in mm^2 and pixels, respectively.

Table 1: Retinal area for different angle values of the field-of-view (FOV), according to [37].

FOV	**Retinal Area** (mm^2)
30°	56.4
40°	99.2
45°	124.8
50°	153.1

$$\alpha = K_0 \left[\frac{A^{\theta}_{mm^2}}{A_{px^2}} \right]^{1/2} \tag{1}$$

The value of $A^{\theta}_{mm^2}$ depends on the FOV of the input image, which is defined by the so-called *external angle view of the fundus camera*. Table 1 shows different values of $A^{\theta}_{mm^2}$ for FOV typical values. The value of A_{px} is easily calculated from the input image, counting the number of actual retinal pixels. The value chosen for the work resolution is $K_0 = 25\, px/mm$. This value is not critical, but should be low enough to eliminate some artifacts present at higher resolutions and high enough so that the fovea and OD do not lose details of interest.

In order to make the segmentation of each structure independent of the type of eye, each image is checked: if it does not match the type of eye established by default (left), it will be horizontally flipped. The left eye criterion was chosen arbitrarily. The method used to automatically determine the type of eye is described in [7].

Finally, in order to use the maximum range of each RGB channel, a normalization based on contrast stretching is applied, that is, a linear transformation $f_{Ch} : [min_{ret}, max_{ret}] \rightarrow [0, 255]$, where min_{ret} and max_{ret} represent the minimum and maximum intensity values, respectively, of the image channel Ch for a given image.

4.2 Optic disc model

In a retinal image, the optic disc, also called *papilla*, has a bright oval shape and contains the output point of the major blood vessels that supply the retina (see Fig. 1). It also contains a rounded area located approximately in its center, called *optic cup*, which represents the brightest area of the retina in the absence of noise. More specifically, in relation to the points that define the OD contour, we can classify them into three categories: border points, crossing points and noisy points.

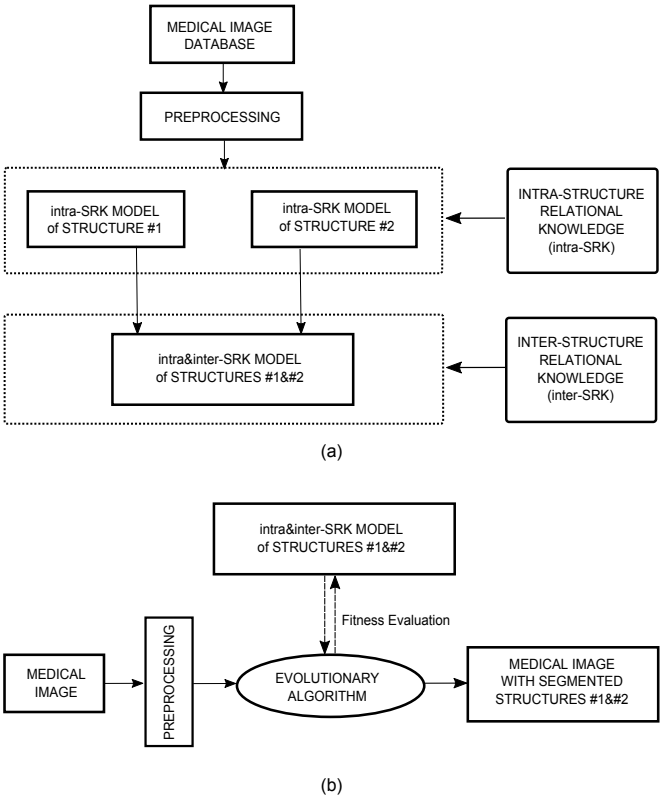

Fig. 2: Block diagram associated with the generic methodology proposed and particularized to two structures: (a) learning the intra&inter-SRK model, (b) using the learned model to simultaneously segment two anatomical structures in a medical image.

A *border point* is characterized by having a neighborhood divided into two zones of high contrast (OD region and retinal background). A *crossing point* is defined by the intersection of a vessel with the OD contour. Finally, because real images will contain noise, all those OD contour points that can not be characterized as border or crossing points will be called *noisy points*. For example, an OD contour point that is not a crossing point and whose neighborhood is blurred will be a noisy point.

Next, we propose making an estimate of the probability p that an OD contour point, according to its position, belongs to the set of border points. In order to estimate N_p probabilities, being N_p the number of regularly spaced points that are evaluated in each elliptical OD contour, we propose algorithm 1. The algorithm procedure is as follows: first of all, as input information, a retinal image set is used, $\mathbf{I}_i$, $i = 1, ..., N$, in which the OD contour ground truth, $\mathbf{Cnt}_{OD_i}$, and fovea center, $\mathbf{C}_{F_i}$, of each image are known. Next, an external `for-loop` visits the entire set of images and, for each of them, three different stages are performed: (i) preprocessing; (ii) extraction of the vessel network; and (iii) evaluation of the probability that each OD contour point, depending on its position, is a border point (internal `for-loop`). Finally, the average probabilities are calculated for each point of the OD contour.

The preprocessing stage uses the steps described in Sect. 4.1: (i) input image normalization; (ii) normalized image transformation into a smaller image with standard resolution K_0; and (iii) if it applies, transformed image horizontal flipping in order to unify the type of eye (left). Additionally, the RGB image resulting from the latter step is used to store the green channel I_G that is transformed into a grayscale image $\mathbf{I}_{GS}$ (weighted sum of the three RGB channels). Next, a rough segmentation of the vessel network $\mathbf{V}$ is performed using I_G as input and the vessel detection method described in [7]. There is experimental evidence in the literature on the high contrast between vessels and background for the green channel [38]. The rest of the algorithm works with I_{GS}.

In order to facilitate the definition of the OD model, an elliptical shape is assumed for the OD contour. This approximation is common in the literature [39, 12, 40, 41]. That is why, in line 5 of algorithm 1, the actual OD contour provided by the expert is approximated by an ellipse, e_{OD} (see Fig. 3.a). The probability that each

Algorithm 1 Pseudo-code to obtain the OD model.

Inputs
$\mathbf{I}_i$, input image set ($i = 1, ..., N$)
K_0, work resolution
eye, type of eye (left)
$\mathbf{Cnt}_{OD_i}$, OD contour ground truth for the i-th image
$\mathbf{C}_{F_i}$, fovea center ground truth for the i-th image
δ, distance from OD ellipse (e_{OD}) to auxiliary ellipse (e_{aux})
N_p, Number of sampling points in e_{OD} and e_{aux}
$n+1$, Number of neighborhood points to check in e_{aux}
Output
$\mathbf{M}_{OD}$, OD model

(01) $\mathbf{t}$:=$[N, ..., N]_{1\times N_p}$;
(02) **for** i:=1 **to** N
(03) $[\mathbf{I}_{GS}, \mathbf{I}_G, \mathbf{Cnt}_{OD}, \mathbf{C}_F]$:=Preprocess$(\mathbf{I}_i, \mathbf{Cnt}_{OD_i}, \mathbf{C}_{F_i}, eye, K_0)$;
(04) $\mathbf{V}$:=Segment-Vessels$(\mathbf{I}_G)$;
(05) e_{OD}:=Approx-Ellipse$(\mathbf{Cnt}_{OD})$;
(06) e_{aux}:=Build-Ellipse(e_{OD}, δ);
(07) $[P_{OD}, P_{aux}]$:=Obtain-Cut-Pts$(e_{OD}, e_{aux}, \mathbf{C}_F)$;
(08) $[\widetilde{\mathbf{e}}_{OD}, \widetilde{\mathbf{e}}_{aux}]$:=Sample-Ellipses$([e_{OD}, P_{OD}], [e_{aux}, P_{aux}], N_p)$;
(09) **for** j:=1 **to** N_p
(10) **if** $\widetilde{\mathbf{e}}_{OD}(j) \in$ CrossingPoint
(11) $\mathbf{p}(i, j)$:=0;
(12) **else if** $\widetilde{\mathbf{e}}_{OD}(j) \in$ BorderPoint
(13) $\mathbf{p}(i, j)$:=1;
(14) **else**
(15) $\mathbf{p}(i, j)$:=0;
(16) $\mathbf{t}(j)$:=$\mathbf{t}(j) - 1$;
(17) **end-if**
(18) **end-for**
(19) **end-for**
(20) $\mathbf{M}_{OD}$:=$[\sum_{i=1}^{N}(\mathbf{p}(i, 1)/\mathbf{t}(1), ..., \sum_{i=1}^{N}(\mathbf{p}(i, N_p)/\mathbf{t}(N_p))]$;

OD contour point is a border point depends on its position. Therefore, it is necessary to establish a reference point in the elliptical contour that allows us to unequivocally define the position of the rest of points in the contour, independently of the degree of inclination of the ellipse major axis. For this (line 7), the intersection points of e_{OD} and e_{aux} with the straight line joining the OD and fovea centers are calculated (see Fig. 3.b). These points, P_{OD} and P_{aux}, will mark the initial point (reference point) of sampling and storage of N_p regularly spaced points in e_{OD} and e_{aux}, respectively (line 8). The purpose of e_{aux} is explained below.

Three conditions are checked in an if-elseif-else structure (lines 10-17) to store the probability that a point in e_{OD} is a border point according with its position. First, using the binary image of the segmented vessels $\mathbf{V}$, it is checked if the current point belongs to a crossing point. If so, it is assigned a zero probability of belonging to border point. If not, the intensity of the current point is compared with those of the $n+1$ neighboring points that are located in an auxiliary ellipse e_{aux}. This ellipse is built concentrically and externally to e_{OD} and is separated from it by a distance δ (see Fig. 3.b). So, if the intensity of the current point is greater than that of all its $n+1$ nearest neighbors located in e_{aux}, the current point will be assigned a probability equal to one of belonging to a border point. This heuristic is based on the property that a border points is characterized by having a neighborhood divided into two zones of high contrast: the papillary zone (brighter) and the retinal zone (less bright). Therefore, the membership of the j-th ellipse point, $\widetilde{\mathbf{e}}_{OD}(j)$, to a border point can be expressed mathematically by Eq. (2).

$$\widetilde{\mathbf{e}}_{OD}(j) \in P_{border} \Longleftrightarrow \begin{cases} \mathbf{I}_{GS}(\widetilde{\mathbf{e}}_{OD}(j)) > \mathbf{I}_{GS}(\widetilde{\mathbf{e}}_{aux}(k)), \\ \forall k \in \{j - \frac{n}{2}, .., j, .., j + \frac{n}{2}\} \end{cases} \tag{2}$$

Finally, if the current point does not fulfill any of the two conditions previously mentioned, it will be labeled as a noisy point and its contribution to the calculation of the final average probability will be ignored. For this, a zero probability is assigned (line 15) and, in addition, this point is not counted for the total computation of points used to calculate the average probability (line 16). Figure 3.c shows an example of OD elliptical contour point labeling.

The MESSIDOR database ($N = 1200$) was used to build the probability model. The number of regularly spaced points was $N_P = 140$, the distance between e_{OD} and e_{aux} was $\delta = 2$ pixels and the number of neighbor points ($n+1$) in e_{aux} was $n = 8$. These three values were experimentally obtained. However, it should be taken into account that N_p, δ and n are related to K_0, in such a way that the former must increase when the latter does and vice versa.

Figure 4.a shows the probability curve obtained by applying algorithm 1 (see continuous line). The x-axis represents the location of the N_p sampled points, starting from P_{OD} and traveling the ellipse perimeter in a clockwise direction. The y-axis represents the average probability of each point being a border point. It can be observed that the peak values correspond to the nasal and temporal zone, that is, where there is a lower concentration of vessels (see Fig. 1) and, therefore, $p \to 1$. On the other hand, the valley values correspond to the superior and inferior zone ($p \ll 1$), that is, the zones where the majority of the vessels leave the OD and, subsequently, branch out through the rest of the retina. Finally, a Fourier series expansion with ten harmonics is used to smooth and filter the high frequency noise of the obtained probability curve. The resulting curve is shown in Fig. 4.b. Henceforth, the probability vector $\mathbf{M}_{OD}$ that orderly stores the different average probabilities that a point of the papillary contour is a border point will be called the *OD model*. Figure 4.b also shows the average probability $(1-p)$ of belonging to a crossing point (see dashed line).

Once the OD model ($\mathbf{M}_{OD}$) is obtained, the question is how to evaluate a model instance, $\widehat{\mathbf{M}}_{OD}$, that is, how to evaluate an ellipse of parameters $(\widehat{\mathbf{C}}_{OD}, \widehat{a}, \widehat{b}, \widehat{\rho})$

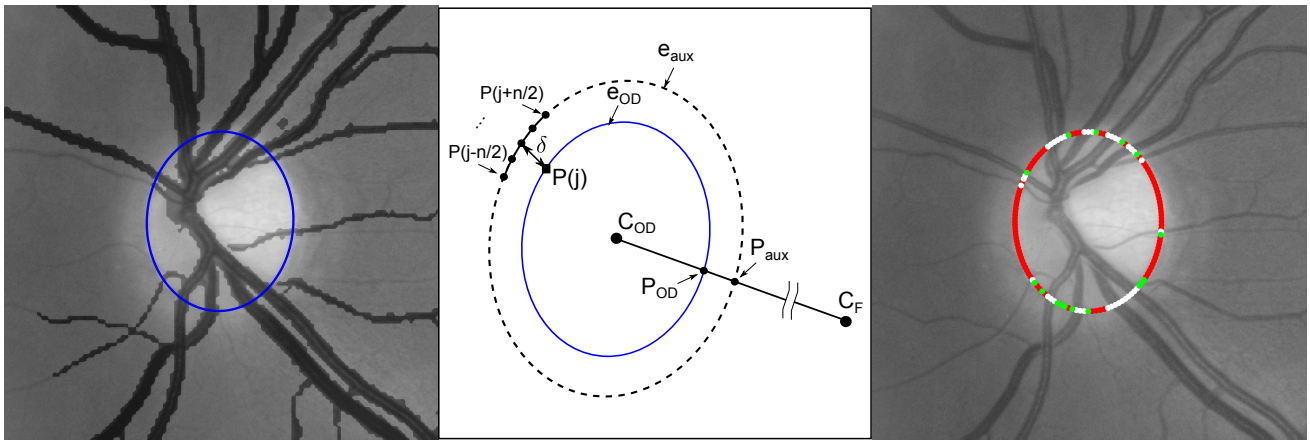

(a) (b) (c)

Fig. 3: Example showing different representations of the OD contour: (a) approximating the OD contour by an ellipse, e_{OD} (the vessel segmentation is also shown); (b) the $n+1$ nearest points belonging to e_{aux} that are used to evaluate the probability that $P(j)$ is a border point (the cut points, P_{OD} and P_{aux}, are also shown, being C_F the fovea center); (c) example of classification of the OD contour points as border points (red), crossing points (white) or noisy points (green). See color figure online.

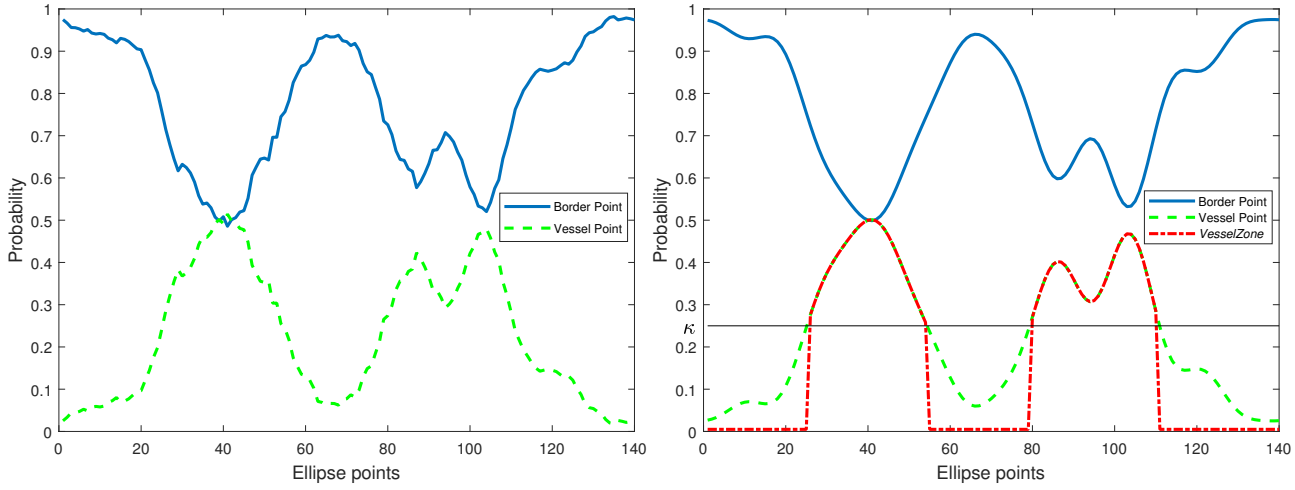

(a) (b)

Fig. 4: The OD model ($\mathbf{M}_{OD}$) is represented by the curve that stores the average probability that each OD-ellipse point is a border point: (a) $\mathbf{M}_{OD}$ obtained by algorithm 1 (blue line); (b) $\mathbf{M}_{OD}$ obtained as a result of approximating the original M_{OD} by a Fourier series expansion with 10 harmonics (blue line). In both subfigures, it is also shown the curve that stores the average probability that each OD-ellipse point is a crossing point (green line). The vessel zone (red line) is shown in (b). See color figure online.

in a given retinal image $\mathbf{I}$, being $\widehat{\mathbf{C}}_{OD}$, $\widehat{a}$ and $\widehat{b}$ the center, major and minor semi-axis the ellipse, respectively, and $\widehat{\rho}$ the angle of the ellipse major axis with the x-axis. The answer to that question can be formalized by means of Eq. (3), where $\widehat{\mathbf{C}}_F$, which is also part of the model instance, is a fovea center prediction (see Fig. 3.b), and $\widehat{f}_{OD}$ is an evaluation function.

$$\widehat{\mathbf{M}}_{OD} = \widehat{f}_{OD}(\mathbf{I}, \widehat{\mathbf{C}}_{OD}, \widehat{a}, \widehat{b}, \widehat{\rho}, \widehat{\mathbf{C}}_F) \tag{3}$$

We propose algorithm 2 as a function $\widehat{f}_{OD}$, where the parameters K_0, eye, δ, and N_p keep the same values as those used to construct $\mathbf{M}_{OD}$. The rest of the algorithm runs quasi-parallel to algorithm 1, with the only

difference that the probabilities to consider here correspond to the input ellipse points and are evaluated as follows. If an ellipse point, j, is a border point (see Eq. (2)), then it is assigned the j-th probability of the OD model ($\mathbf{M}_{OD}$). If the j-th point is a noisy point, a zero value is assigned as a penalty value, thus maximizing the error value associated with this type of points (this will be clarified later in Sect. 4.5.2). Finally, if the j-th point is a crossing point, the probability value is assigned depending on whether that point belongs or not to a zone denominated the *vessel zone,* that is, a region located in the superior and inferior zone of the OD contour (see Fig. 4.b). The criterion given by Eq. (4) establishes when an ellipse point belongs to the vessel zone, where $(1 - \mathbf{M}_{OD}(j))$ represents, according to the OD model, the probability that a point is a crossing point, and $\kappa \in [min(1 - \mathbf{M}_{OD}(j)), max(1 - \mathbf{M}_{OD}(j))]$ is a fixed threshold, chosen by the user, which establishes the width of the vessel zone.

$$(\widetilde{\mathbf{e}}_{OD}(j) \in \text{Vessel\_Zone}) \Longleftrightarrow (1 - \mathbf{M}_{OD}(j)) \geq \kappa \qquad (4)$$

Then, if the j-th point is a crossing point and belongs to the vessel zone, it will be assigned a probability $(1 - \mathbf{M}_{OD}(j))$ (lines 13-14 of algorithm 2). Otherwise, it will be considered a noisy point and will be assigned a zero probability (lines 15-16). The purpose of defining the vessel zone is to penalize ellipses that follow the path marked by the borders associated with vessels in the temporal or nasal area of the OD contour. The higher κ is, the narrower the vessel zone will be (see Fig. 4.b) and, therefore, the lower the possibility of selecting ellipses with the mentioned problem. However, if we assign to κ the maximum value, the width of the vessel zone will be zero and, therefore, all the crossing points will be labeled as noisy points. Taking into account both factors, we experimentally obtained the best results for $\kappa = 0.4$.

Finally, in order to assess how close an OD instance (ellipse in the image) is to the OD model, it will be sufficient to evaluate Eq. (5), where f_{errOD} can be any error function, chosen by the user, that computes the error between $\mathbf{M}_{OD}$ and $\widehat{\mathbf{M}}_{OD}$.

$$error_{OD} = f_{errOD}(\mathbf{M}_{OD}, \widehat{\mathbf{M}}_{OD}) \qquad (5)$$

Algorithm 2 Pseudo-code to evaluate an OD model instance.

Inputs
- $\mathbf{I}$, input image
- $(\widehat{\mathbf{C}}_{OD}, \widehat{a}, \widehat{b}, \widehat{\rho})$, parameters of the ellipse to evaluate (instance)
- $\widehat{\mathbf{C}}_F$, fovea center
- κ, width of the vessel zone
- $(K_0$, eye, δ, N_p, $n)$, same parameters and values as the... parameters defined in algorithm 1

Output
- $\widehat{\mathbf{M}}_{OD}$, evaluation of the OD model instance

```
(01) [I_GS, I_G]:=Preprocess(I, eye, K_0);
(02) V:=Segment-Vessels(I_G);
(03) [e_OD, e_aux]:=Build-Ellipses([Ĉ_OD, â, b̂, ρ̂], δ);
(04) [P_OD, P_aux]:=Obtain-Cut-Pts(e_OD, e_aux, Ĉ_F);
(05) [ẽ_OD, ẽ_aux]:=Sample-Ellipses([e_OD, P_OD], [e_aux, P_aux], N_p);
(06) for j:=1 to N_p
(07)  if (ẽ_OD(j) ∈ BorderPoint);
(08)   M̂_OD(j):=M_OD(j);
(09)  end-if
(10)  if ẽ_OD(j) ∉ CrossingPoint) & (ẽ_OD(j) ∉ BorderPoint
(11)   M̂_OD(j):=0;
(12)  end-if
(13)  if ẽ_OD(j) ∈ CrossingPoint) & (ẽ_OD(j) ∈ VesselZone(κ)
(14)   M̂_OD(j):=1 − M_OD(j);
(15)  else if ẽ_OD(j) ∈ CrossingPoint) & (ẽ_OD(j) ∉ VesselZone(κ)
(16)     M̂_OD(j):=0;
(17)    end-if
(18)  end-if
(19) end-for
```

4.3 Fovea model

In a retinal image, intensity levels in the fovea area grow following the direction of an imaginary beam located in the fovea center (see Fig. 1). Here we propose to built a fovea model characterizing this intensity variation pattern and using the angles and modules of the vectors resulting from applying the gradient operator to the fovea region.

Algorithm 3 shows the steps followed in order to build a model that approximates the above-mentioned fovea pattern. A set of retinal images, $\mathbf{I}_i$, $i = 1, ..., N$, is used as input information, where the actual fovea center $\mathbf{C}_{F_i}$ is known for each image. Next, a preprocessing stage is applied: First, a green channel normalization I_G of the input image is done. There is evidence in the literature about the green channel offers the greatest contrast to segment the fovea [25, 42]. Second, the resolution of the normalized green channel is transformed to the work resolution K_0. Third, if applicable, a horizontal flipping is used in order to unify the type of eye (left). Next, a `for-loop` goes through all the images and, in each of them, the gradient operator is applied to the sub-window, $\mathbf{W}_F$, of size $L \times L$ and centered on the actual fovea center. Two matrices, $\mathbf{Gx}$(i) and $\mathbf{Gy}$(i), $i = 1, ..., N$, are obtained, each one containing the respective values of the components x and y of the gradient vectors. Once all the images have been processed, the average value of each component, $\mathbf{Gx}$ and $\mathbf{Gy}$, is calculated. Finally, the matrices $\mathbf{M}_{F_M}$ and $\mathbf{M}_{F_A}$ store, respectively, the result of calculating the modulus and angle of the gradient vectors from $\mathbf{Gx}$ and $\mathbf{Gy}$. Henceforth, the set of matrices $\mathbf{M}_F = \{\mathbf{M}_{F_M}, \mathbf{M}_{F_A}\}$ will be called the *fovea model*.

Algorithm 3 Pseudo-code to obtain the fovea model.

Inputs
$\mathbf{I}_i$, input image set ($i = 1, ..., N$)
K_0, work resolution
eye, type of eye (left)
$\mathbf{C}_{F_i}$, fovea center ground truth in i-th image
L, size of fovea sub-window ($L \times L$)
Output
$\mathbf{M}_F$, fovea model

(01) **for** i:=1 **to** N
(02) $[\mathbf{I}_G, \mathbf{C}_F]$:=Preprocess($\mathbf{I}_i, \mathbf{C}_{F_i}, eye, K_0$);
(03) $\mathbf{W}_F$:=Extract-Fovea-Subwindow($\mathbf{I}_G, \mathbf{C}_F, L$);
(04) [$\mathbf{Gx}$(i), $\mathbf{Gy}$(i)]:=Compute-Gradient($\mathbf{W}_F$);
(05) **end-for**
(06) $\mathbf{Gx}$:=Compute-Means($\mathbf{Gx}(1), ..., \mathbf{Gx}(N)$);
(07) $\mathbf{Gy}$:=Compute-Means($\mathbf{Gy}(1), ..., \mathbf{Gy}(N)$);
(08) $\mathbf{M}_{F_M}$:=Compute-Modules($\mathbf{Gx}, \mathbf{Gy}$);
(09) $\mathbf{M}_{F_A}$:=Compute-Angles($\mathbf{Gx}, \mathbf{Gy}$);
(10) $\mathbf{M}_F$:=[$\mathbf{M}_{F_M}, \mathbf{M}_{F_A}$];

In order to build the fovea model, we used a subset of $N = 546$ MESSIDOR images without macular pathologies. The sub-window size chosen was $L = 27$ pixels (at resolution K_0). This value is obtained from considering that the typical fovea radius is between 2/3 and 2/4 of one R_{OD} [43, 25, 44]. The R_{OD} value in pixels, at resolution K_0, is obtained from Eq. (6), where $R_{OD,mm} = 0.925\ mm$ is the mean radius of the optic disc in mm [1].

$$R_{OD} = K_0 \cdot R_{OD,mm} \tag{6}$$

Figure 5 shows the information of interest related to the obtained fovea model. In particular, the figure shows the matrices of angles (Fig. 5.c) and modules (Fig. 5.d) of the average vector field (Fig. 5.b) that result from applying the gradient operator to the fovea region encompassed by $\mathbf{W}_F$ (see Fig. 5.a) in the set of images used.

Once the fovea model ($\mathbf{M}_F$) is obtained, the question is how to evaluate a model instance, $\widehat{\mathbf{M}}_F$. That is, given a retinal image, $\mathbf{I}$, how can an image sub-window of size $L \times L$ and centered on a point $\widehat{\mathbf{C}}_F$ be evaluated. The answer to that question can be formalized by Eq. (7), where $\widehat{f}_F$ is an evaluation function.

$$\widehat{\mathbf{M}}_F = \hat{f}_F(\mathbf{I}, \widehat{\mathbf{C}}_F) \tag{7}$$

We propose algorithm 4 as a function $\widehat{f}_F$, where the parameters K_0, eye and L keep the same values as those used to build $\mathbf{M}_F$. The rest of the algorithm runs quasi-parallel to algorithm 3, with the only difference that the gradient vectors evaluated here correspond to the area covered by the sub-window centered on the point $\widehat{\mathbf{C}}_F$ of the input image. Finally, in order to assess how close an instance (sub-window in the image) is to the fovea model, it will be sufficient to evaluate Eq. (8), where f_{errF} can be any error function, chosen by the user, that computes the error between $\mathbf{M}_F$ and $\widehat{\mathbf{M}}_F$.

$$error_F = f_{errF}(\mathbf{M}_F, \widehat{\mathbf{M}}_F) \tag{8}$$

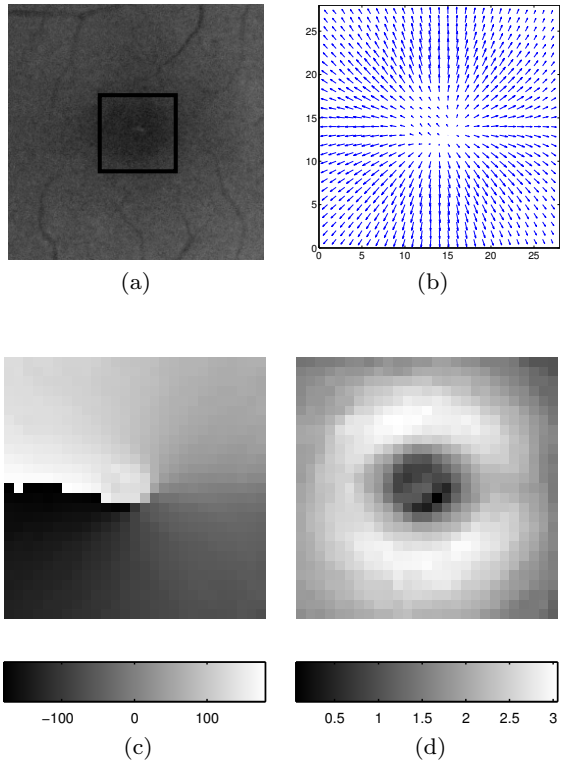

Fig. 5: Fovea model based on the computation of angles and modules of the average vector field resulting from applying the gradient operator to the fovea region of a subset of MESSIDOR healthy images: (a) partial view of a retina image (green channel) in which the sub-window $\mathbf{W}_F$ centered on the actual fovea center is shown; (b) average gradient vector field; (c) angles of the average gradient vector field; (d) modules of the average gradient vector field.

4.4 OD-fovea model

The OD intra-SRK could be used to just segment the OD and, similarly, the fovea intra-SRK, to just segment the fovea. However, we should use all the available relational knowledge, intra- and inter-SRK, to increase the robustness of the segmentation process of both structures. In this section, we describe how to merge the two previously built intra-SRK models, adding the relational knowledge that exists between OD and fovea, to create an OD-fovea model. Then, as we will see in Section 4.5, the resulting relational model will be used by a segmentation method (evolutionary algorithm) to simultaneously segment the OD and fovea.

First, it is known that the average distance between the centers of the OD and fovea, $\overline{D}(\mathbf{C}_{OD}, \mathbf{C}_F)$, is ap-

Algorithm 4 Pseudo-code to evaluate a fovea model instance.

Inputs
I, input image
(K_0, *eye*, L), same parameters and values as the parameters... defined in algorithm 3
$\widehat{\mathbf{C}}_F$, center of the sub-window $\widehat{\mathbf{W}}_F$ to evaluate as fovea instance
Output
$\widehat{\mathbf{M}}_F$, evaluation of the fovea model instance

(01) $[\mathbf{I}_G]$:=Preprocess($\mathbf{I}, eye, K_0$);
(02) $\widehat{\mathbf{W}}_F$=Build-Subwindow($\mathbf{I}_G$,$\widehat{\mathbf{C}}_F$,L)
(03) $[\widehat{\mathbf{Gx}}, \widehat{\mathbf{Gy}}]$:=Compute-Gradient($\widehat{\mathbf{W}}_F$);
(04) $\widehat{\mathbf{M}}_{F_M}$:=Compute-Modules($\widehat{\mathbf{Gx}}, \widehat{\mathbf{Gy}}$);
(05) $\widehat{\mathbf{M}}_{F_A}$:=Compute-Angles($\widehat{\mathbf{Gx}}, \widehat{\mathbf{Gy}}$);
(06) $\widehat{\mathbf{M}}_F = [\widehat{\mathbf{M}}_{F_M}, \widehat{\mathbf{M}}_{F_A}]$;

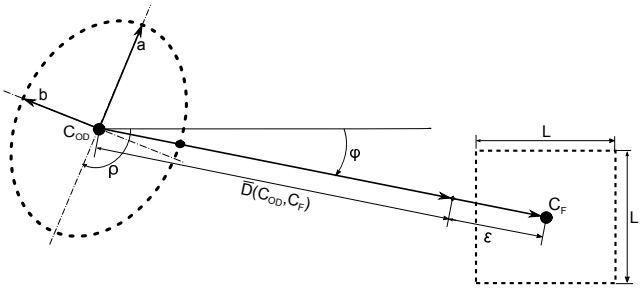

Fig. 6: Schematic representation of the OD-fovea model.

proximately five times R_{OD} [45], that is:

$$\overline{D}(\mathbf{C}_{OD}, \mathbf{C}_F) \approx 5R_{OD} \tag{9}$$

Note that $\overline{D}(\mathbf{C}_{OD}, \mathbf{C}_F)$ is a constant that can be computed, at work resolution K_0 using Eqs. (6) and (9). Therefore, the distance between the centers of the OD and fovea for any image can be expressed using Eq. (10), where ε is a positive or negative distance increment, which represents a possible deviation from $\overline{D}(\mathbf{C}_{OD}, \mathbf{C}_F)$ of the actual distance between the OD and fovea centers for a given image.

$$D(\mathbf{C}_{OD}, \mathbf{C}_F) = \overline{D}(\mathbf{C}_{OD}, \mathbf{C}_F) + \varepsilon \tag{10}$$

Finally, it is also known that, the OD and fovea center are not usually horizontally aligned. There exists a positive or negative angle φ between the horizontal and the segment that joins both centers [46, 26]. Figure 6 illustrates and summarizes the resulting OD-fovea model.

Once the OD-fovea model is built, the question is how to evaluate an instance ($\widehat{\mathbf{C}}_{OD}$,$\widehat{a}$,$\widehat{b}$,$\widehat{\rho}$,$\widehat{\varphi}$,$\widehat{\varepsilon}$) of such a model. First, from the tuple ($\widehat{\mathbf{C}}_{OD}, \widehat{\varphi}, \widehat{\varepsilon}$), it is direct to obtain the components of $\widehat{\mathbf{C}}_F$ using Fig. 6:

$$\begin{aligned} \widehat{C}_{Fx} &= \widehat{C}_{ODx} + (\overline{D}(C_{OD}, C_F) + \widehat{\varepsilon}) \cdot \cos(\widehat{\varphi}) \\ \widehat{C}_{Fy} &= \widehat{C}_{ODy} + (\overline{D}(C_{OD}, C_F) + \widehat{\varepsilon}) \cdot \sin(\widehat{\varphi}) \end{aligned} \tag{11}$$

Therefore, the evaluation of a relational model instance can be done by Eq. (12), where $\widehat{f}_{OD}$ and $\widehat{f}_F$ are computed using algorithms 2 and 4, respectively.

$$\begin{aligned} \widehat{\mathbf{M}}_{OD\_F} &= \widehat{f}_{OD\_F}(\mathbf{I}, \widehat{\mathbf{C}}_{OD}, \widehat{a}, \widehat{b}, \widehat{\rho}, \widehat{\varphi}, \widehat{\varepsilon}) \\ &= [\widehat{f}_{OD}(\widehat{\mathbf{C}}_{OD}, \widehat{a}, \widehat{b}, \widehat{\rho}, \widehat{\mathbf{C}}_F),\ \widehat{f}_F(\widehat{\mathbf{C}}_F)] \end{aligned} \tag{12}$$

Finally, in order to evaluate how close the instance is to the relational model, it will be enough to use Eq. (13), where ω_{OD} and ω_F are two weighting factors chosen by the user, and f_{errOD} and f_{errF} are computed from Eqs. (5) and (8), respectively.

$$\begin{aligned} error_{OD\_F} &= f_{errOD\_F}(\mathbf{M}_{OD\_F}, \widehat{\mathbf{M}}_{OD\_F}) \\ &= \omega_{OD} \cdot f_{errOD}(\mathbf{M}_{OD}, \widehat{\mathbf{M}}_{OD}) + \\ &\quad \omega_F \cdot f_{errF}(\mathbf{M}_F, \widehat{\mathbf{M}}_F) \end{aligned} \tag{13}$$

4.5 Evolutionary algorithm

The advantage of the relational model proposed in the previous section is that it allows us to transform the problem of the simultaneous segmentation of the OD and fovea into a new problem consisting of minimizing the expression (13), taking into account Eq. (11). This minimization problem can be formalized by Eq. (14).

$$\min_{(\mathbf{C}_{OD}, a, b, \rho, \varphi, \varepsilon)} error_{OD\_F} \tag{14}$$

Since the problem thus defined depends on the optimization of seven real parameters ($\mathbf{C}_{OD}$ has two components), it can not be solved by brute force. Therefore, an evolutionary algorithm is proposed instead. Throughout this section, the necessary steps to address an optimization problem with this type of algorithms are described: (i) representation of the individuals, (ii) definition of the fitness function, and (iii) instantiation of the evolutionary algorithm.

4.5.1 Representation of individuals

Each individual will encode an instance of the OD-fovea relational model defined in Sect. 4.4. Thus, an individual (chromosome) is defined as a fixed length vector, where each component (gene) is associated with each of the parameters of the relational model. Table 2 shows the correspondence between each vector component and each model parameter, as well as the definition domain of each parameter. All the values shown in the definition domains are calculated at work resolution ($K_0 = 25$). In particular, we assumed that each parameter a and b is modeled by a normal distribution with mean and standard deviation ($\mu_a = 24.3, \sigma_a = 2.2$) and ($\mu_b = 22.2, \sigma_b = 2.2$), respectively. These means and standard deviations were calculated from the 1200

MESSIDOR images. The approximated definition domain of each one of these two parameters was built considering the property that about 99.7% of values drawn from a normal distribution are within three standard deviation away from the mean. The domain for parameter ρ was defined without restrictions and, for parameter φ, a criterion similar to that employed in [26] was used. Finally, in relation to parameter ε, its definition domain was chosen in such a way that the distance between the centers of the OD and fovea can vary $\pm 1 R_{OD}$ with respect to its average distance (see Eq. (9)).

4.5.2 Fitness function

In a first approximation, the fitness function is defined by Eq. (13). Therefore, it will be necessary to define two error functions, f_{errOD} and f_{errF}. Here, we propose the functions given by Eqs. (15) and (16), where $\mathbf{max}_{OD}(i) = \max\{\mathbf{M}_{OD}(i), 1 - \mathbf{M}_{OD}(i)\}$.

$$f_{errOD} = \frac{\sum_{i=1}^{N_p} \left(\mathbf{max}_{OD}(i) - \widehat{\mathbf{M}}_{OD}(i) \right)}{\sum_{i=1}^{N_p} \left(\mathbf{max}_{OD}(i) \right)} \tag{15}$$

$$f_{errF} = \frac{\sum_{i=1}^{L} \sum_{j=1}^{L} \mathbf{M}_{F_M}(i,j) \left| (\mathbf{M}_{F_A}(i,j) - \widehat{\mathbf{M}}_{F_A}(i,j)) \right|}{180 \sum_{i=1}^{L} \sum_{j=1}^{L} \mathbf{M}_{F_M}(i,j)} \tag{16}$$

Note that the value returned by both functions is normalized in $[0, 1]$. In particular, for the OD, the worst case ($f_{errOD} = 1$) corresponds to an ellipse in which none of its points is a border point, that is, $\forall i \widehat{\mathbf{M}}_{OD}(i) = 0$, and the best case ($f_{errOD} = 0$) is obtained when all the ellipse points are correctly classified, that is, $\forall i \, \widehat{\mathbf{M}}_{OD}(i) = \mathbf{max}_{OD}(i)$. Whilst, for the macula, the worst case ($f_{errF} = 1$) is reached when the absolute error evaluated in each sum of the numerator always returns the maximum error of angle (180°), and the best case ($f_{errF} = 0$), when the model and instance angle matrices match, that is, $\forall ij \, \widehat{\mathbf{M}}_{F_A}(i,j) = \mathbf{M}_{F_A}(i,j)$.

However, we can further refine the definition of our fitness function. In particular, the intra-SRK can also be used to establish constraints on the model parameters or other derived parameters. Next, we analyze the statistical knowledge associated with ρ, one of the model parameters, and two derived parameters: ellipse area (A) and difference between ellipse semi-axes (λ). The choice of these three parameters is based on the following domain knowledge: (a) the major axis of the OD standard gold ellipses tends to be vertically oriented ($\rho \approx 90°$); (b) given that the contour of the optic cup can present a pattern similar to the OD contour, an area constraint is used to discard possible false positives; (c) the ellipse major semi-axis is always larger than or equal to the minor semi-axis and, in addition, the eccentricity of the OD standard gold ellipses tends to be small. Table 3 shows the estimated probability density function and definition domain (X_o, X_f) of each parameter, considering the 1200 MESSIDOR images at work resolution ($K_0 = 25$). The interval extremes (X_o, X_f) were chosen assuming that 95% of the values extracted from each of the estimated distributions are within the mentioned interval.

The idea is to use each interval (X_o, X_f) to define constraints that allow us to penalize genetic ellipses whose parameters ρ, A and β move away from the range of the mentioned intervals. The most immediate way to use these constraints in the optimization problem is to incorporate them as penalties within the function that evaluates the error of the OD model, that is, in f_{errOD}. To do this, three penalty functions are defined, $P(\rho)$, $P(A)$, and $P(\lambda)$, following the scheme of the generic function given by Eq. (17), where (X_0, X_f) is given by Table 3 for each value of $X \in \{\rho, A, \lambda\}$.

$$P(X) = \begin{cases} 0 & \text{if } X \epsilon (X_o, X_f) \\ 10 \cdot \frac{\min\{|X - X_o|, |X - X_f|\}}{(X_f - X_o)} & \text{other case} \end{cases} \tag{17}$$

As we are addressing a minimization problem, the problem of minimizing f_{errOD} will be transformed into the problem of minimizing the function given by Eq. (18), where the constraints are taken into account.

$$f^{(c)}_{errOD} = f_{errOD} + P(\rho) + P(A) + P(\lambda) \tag{18}$$

Finally, the fitness function to be minimized by the evolutionary algorithm is given by Eq. (19), where w_{OD} and w_F contributed with the same value (equal to 0.5), given that both the OD and fovea search have the same importance in the segmentation process.

$$F = \omega_{OD} \cdot f^{(c)}_{errOD} + \omega_F \cdot f_{errF} \tag{19}$$

4.5.3 Differential evolution

In this work, we propose differential evolution (DE) [47] as a candidate to play the role of evolutionary algorithm (EA). Several reasons motivate this decision. First of all, DE is simple and straightforward to implement and yields promising results. Second, DE manages in a natural way individuals expressed as fixed dimension real vectors. Third, the DE control parameter space complexity is low compared with some of the most competitive real parameter optimizers [48]. Finally, DE has already been successfully used for segmentation of images

Table 2: Information associated with each gene encoded in a chromosome, including its description and domain of definition. See Section (4.5.1) for more information.

#Gen	Gen	Description	Domain of definition
1	C_{ODx}	Coordinate x of $\mathbf{C}_{OD}$	$[\min(x), \max(x)]$ / $\exists y\ p(x,y) \in$ retina
2	C_{ODy}	Coordinate y of $\mathbf{C}_{OD}$	$[\min(y), \max(y)]$ / $\exists x\ p(x,y) \in$ retina
3	a	Major semi-axis of ellipse	$[\mu_a - 3\sigma_a, \mu_a + 3\sigma_a] = [17.7, 30.9]$
4	b	Minor semi-axis of ellipse	$[\mu_b - 3\sigma_b, \mu_b + 3\sigma_b] = [15.6, 28.8]$
5	ρ	Angle$(a, axis_x)$	$[0, 180]^\circ$
6	φ	Angle$(\overline{(\mathbf{C}_{OD}, \mathbf{C}_F)}, axis_x)$	$[-25, 25]^\circ$
7	ε	Deviation from $\overline{D}(C_{OD}, C_F)$	$[-R_{OD}, R_{OD}] = [-23.1, 23.1]$

Table 3: Information associated with the parameters ρ, A and λ, including their estimated probability density functions and definition domains. See Section (4.5.2) for more information.

Variable (X)	Probability density function	(X_o, X_f)
$A = \pi ab$	Normal ($\mu = 1712.3\ px^2$, $\sigma = 317.1\ px^2$)	(2346.5, 1078.1)
$\rho = \text{angle}(a, axis_x)$	Normal ($\mu = 90.6^\circ$, $\sigma = 22.8^\circ$)	(45.0, 136.2)
$\lambda = (a - b)$	Gamma ($A = 2.6817$, $B = 0.7979$)	(0.39, 5.36)

in different medical domains [49, 50, 51, 52]. However, taking into account the type of representation used and the characteristics of the problem to be solved, other EA candidates and their variants could be used, such as genetic algorithms [53], evolution strategies [54] or covariance matrix adaptation-evolution strategies (CMA-ES) [55], or even other metaheuristics, such as particle swarm optimization [56] or biogeography-based optimization [57, 58], among others. In any case, it is important to note that the methodology proposed here to simultaneously segment the OD and fovea is independent of the type of metaheuristic used to tune the seven parameters of the OD-fovea model.

Basically, DE follows the typical stages of an EA (initialization, parent selection, mutation, recombination and survival selection), but it is characterized by a particular implementation of the mutation. There are different DE variants [59]. Here, we selected that denoted by "DE/rand/1/bin", that is, the standard variant (see algorithm 5, where a minimization problem is assumed). Thus, for each individual of the population, $\mathbf{x}_i$, mutation produces a new individual given by Eq. (20), where $\mathbf{x}_p$, $\mathbf{x}_q$, and $\mathbf{x}_r$ are three individuals randomly selected from the population, without replacement and different from $\mathbf{x}_i$; and $F \in [0, 2]$ is a constant chosen by the user and called the *differential weight*.

$$\mathbf{y} = \mathbf{x}_p + F \cdot (\mathbf{x}_q - \mathbf{x}_r) \tag{20}$$

Recombination is done using the different components from $\mathbf{x}_i$ and $\mathbf{y}$ with a probability given by CR, where $CR \in [0, 1]$ is called the *crossover probability*. If the fitness of the resultant child $\mathbf{y}$ is better than $\mathbf{x}_i$, then the first replace the latter in the population. The notation "DE/x/y/z" is interpreted as follows: the label x refers to how the individual playing the role of $\mathbf{x}_p$ in the mutation is selected (in our case, randomly, i.e., "$x = rand$"); the label y denotes how many couples of individuals are involved in the computation of the subtraction shown in Eq. (20) (in our case, "$y = 1$"); and the label z refers to the type of recombination used (in our case, binomial, i.e., "$z = bin$", such as is shown in lines 6-13 of algorithm 5).

Algorithm 5 Pseudo-code of the DE algorithm ("DE/rand/1/bin" variant).

Inputs:
$f : \mathbb{R}^n \to \mathbb{R}$, fitness function to minimize
$CR \in [0, 1]$, crossover probability
$F \in [0, 2]$, differential weight
PS, population size
Output:
$\mathbf{x}^*$, the best individual from final population ($\mathbf{P}$)

```
(01) Initialize-randomly P = {x_1, ..., x_PS}
(02) until (termination-criterion)
(03)   for each x_i ∈ P
(04)     Pick-Randomly {p, q, r} ∈ {1, .., PS}...
          where i ≠ p, i ≠ q, i ≠ r, p ≠ q, p ≠ r, q ≠ r
(05)     Pick-Randomly R ∈ {1, ..., n}
(06)     for each j ∈ {1, ..., n}
(07)       r_j ≡ U(0, 1)
(08)       if r_j < CR or j = R
(09)         y_j = x_pj + F · (x_qj − x_rj)
(10)       else
(11)         y_j = x_ij
(12)       end-if
(13)     end-for
(14)     if f(y) < f(x_i) then x_i = y end-if
(15)   end-for
(16) end-until
```

Table 4 shows the value used for each of the different parameters of the DE-based algorithm. These values were obtained experimentally. Initially, we start with the value recommended for this type of algorithms [47]. Thus, with respect to the population size, PS, we start with a value equal to ten times the number of chromosome genes. However, decreasing the value for population size to 25 and establishing the maximum

Table 4: Values of the parameters used in the DE algorithm.

Parameter	**Value**
DE variant	"DE/rand/1/bin"
Population size (PS)	25
Maximum number of generations (G_{max})	800
Crossover probability (CR)	0.7
Differential weight (F)	0.8
Fitness function	See Eq. (19)
[ω_{OD},ω_F] (see Eq. (19))	$[0.5, 0.5]$

number of generations to 800, the quality of the results obtained did not become worse. Finally, different values were tested for the crossover rate, CR, and the differential weight, F. The pair of values with which we obtained the best results was (CR, F)=$(0.7, 0.8)$.

5 Experimental results and discussion

In order to evaluate the retinal structure segmentation results, there are different indexes in the literature. For example, in OD segmentation, *Jaccard's* (JC) and *Dice's* (D) *coefficients* are frequently used (see Eqs. (21) and (22), respectively), which describe the degree of overlap between the gold standard area, A_{GS}, and the segmented area, A_S, being equal to 1 when the segmentation is perfect. Other indexes like *accuracy*, *true positive fraction* and *false positive fraction* are also typically used. In particular, accuracy (Ac) is determined by dividing the sum of pixels correctly classified as OD and non-OD by the total number of pixels in the image. The true positive fraction (TPF) is obtained by dividing the pixels correctly classified as OD by the total number of OD pixels in the gold standard. The false positive fraction (FPF) is calculated by dividing the pixels misclassified as OD by the total number of non-OD pixels in the gold standard.

$$JC = \frac{|A_{GS} \cap A_S|}{|A_{GS} \cup A_S|} \tag{21}$$

$$D = \frac{2\,|A_{GS} \cap A_S|}{|A_{GS}| + |A_S|} \tag{22}$$

As regards fovea segmentation, the so-called $(\frac{1}{8})R_{OD}$, $(\frac{1}{4})R_{OD}$, $(\frac{1}{2})R_{OD}$ and $1R_{OD}$ criteria are typically used. These criteria are based on evaluating the percentage of cases where the distance between the estimated fovea center and the actual fovea center is less than $(\frac{1}{8})$, $(\frac{1}{4})$, $(\frac{1}{2})$ and 1 R_{OD}, respectively. In our case, these criteria were calculated at work resolution K_0, where R_{OD} is calculated according to Eq. (6).

Finally, sensitivity (Sens) and specificity (Spec) have also been used in order to evaluate both fovea and OD segmentation. The former is defined as the TPF, and the latter, as the true negative fraction (TNF) which is equivalent to 1-FPF. Here it is necessary to mention that, in order to calculate the values of sensitivity and specificity in fovea segmentation, the circles centered in the actual and estimated fovea center were considered as the gold standard and estimated fovea region, respectively. The diameter of both circles is the same and equal to the sub-window size, L, chosen to build the fovea model (see Section 4.3).

In order to make a fair comparison, we should compare our method with other recent methods existing in the literature that simultaneously segment the OD and fovea using both types of knowledge (intra- and inter-SRK). Table 5 shows the results of this comparison. On the one hand, regarding the results obtained in [29], their OD results are slightly better than ours, but our fovea results improve theirs. On the other hand, our results are also competitive compared to those obtained in [30], where a convolutional neural network (CNN) was used (deep learning). It should be noted that the Tan *et al*'s method was evaluated in just 20 images. On the other way, we evaluated our method in a database of 1200 images. As far as the authors know, the work presented in [30] is the only study in which CNNs are applied to the joint segmentation of the OD and fovea in fundus images.

It would also be interesting to compare our simultaneous segmentation method with other methods that also use both types of knowledge but where the segmentation process is done sequentially. Here, there could be two possibilities: (i) the OD is previously localized and is used as a reference to segment the fovea; and (ii) the fovea is previously localized and is used as a reference to segment the OD. However, as far as the authors know, there are no works in the literature that address the second case. Regarding the first case, Table 6 shows the results obtained for comparison. We can say that our results are competitive when the distance threshold considered varies from $2R_{OD}$ to $1/4R_{OD}$, obtaining success rates above 94% with our method. Alternatively, if the threshold $1/8R_{OD}$ is used, the winning method is [25], although the best success rate falls to values of 80% when this very restrictive criterion is used.

We also compare our method with segmentation methods that only use intra-SRK. Here, there are also two possibilities: (i) OD segmentation methods; and (ii) fovea segmentation methods. When we compare our method with these latter two, it is important to note that our method segments two structures (fovea and OD), whereas the other two methods just segment

Table 5: Comparison of our method with other methods that use both types of knowledge (intra- and inter-SRK) to simultaneously segment the OD and fovea. The best results are highlighted in bold.

Method	**Database (#Imag.)**	**Fovea**				**OD**		
		Sens	**Spec**	$\leq \frac{1}{2}R_{OD}$	$\leq 1R_{OD}$	**Sens**	**Spec**	**JC**
[Girard et al. 29]	MESSIDOR (1200)	-	-	94.0%	98.0%	-	-	**0.90**
[Tan et al. 30]	DRIVE (40)	**0.8853**	0.9914	-	-	0.8790	0.9927	0.62
This Work	MESSIDOR (1200)	0.8841	**0.9996**	**97.3%**	**99.0%**	**0.9072**	**0.9995**	0.87

Table 6: Success rate comparison (in %) of our method with other competitive methods that use both types of knowledge but where the segmentation process is done sequentially to obtain the fovea (the OD is previously localized and is used as a reference). All the methods were evaluated using the MESSIDOR database. The best results are highlighted in bold.

Method	**Database**	#images	$\frac{1}{8}R_{OD}$	$\frac{1}{4}R_{OD}$	$\frac{1}{2}R_{OD}$	$1R_{OD}$	$2R_{OD}$
[Yu et al. 24]	MESSIDOR	1200	-	-	95.0	-	-
[Gegundez et al. 25]	MESSIDOR	1200	**80.4**	93.9	96.1	96.9	97.8
[Aquino 27]	MESSIDOR	1136	-	83.0	91.3	98.2	**99.6**
[Kao et al. 26]	MESSIDOR	1200	-	-	**97.8**	98.2	-
This work	MESSIDOR	1200	74.7	**94.1**	97.3	**99.0**	**99.6**

one of them. Table 7 shows the results of comparing our method with OD segmentation methods. As can be seen, our results are only slightly surpassed by [18]. However, a closer analysis of these results reveals that our TPF and FPF values are the lowest. This indicates that our method is the most conservative, that is, it identifies a lower number of actual OD pixels (true positives), but it has the advantage of detecting a smaller number of false positives. This behavior could be motivated by the elliptical shape imposed on our OD model. In contrast, in [18], any irregular geometrical form can be used to approximate the OD contour and, therefore, their OD model is more flexible than ours. At the other extreme, the search used in [10] is even more rigid than our method because the OD contour is approximated by a circumference, and their results are slightly worse than ours. These results reveal that our method could improve OD segmentation if the OD contour was modeled by an irregular geometrical form instead of an ellipse. On the other hand, there are not many methods in the literature that address fovea segmentation using only intra-SRK. The main reason is that the fovea is more difficult to localize than the OD and, therefore, most approaches that segment the fovea use the OD previously localized as a reference. In any case, Table 8 shows the results obtained from comparing one of these methods with our approach. Note that our results continue to be competitive.

In order to provide evidence on the robustness of our method, two more public databases were used: ONHSD and DIARETDB1. Both databases have also been used in the related literature for segmentation and detection method benchmarking. However, as far as the authors know, there are no studies in which simultaneous segmentation of OD and fovea is performed on the mentioned databases. Therefore, our method is compared with methods that just segment one of the two structures. In particular, Tables 9 and 10 show, respectively, the segmentation results obtained for the OD (ONHSD) and fovea (DIARETDB1). It is very important to note that our method was evaluated in the ONHSD and DIARETBD1 databases using the same models and configuration of parameters as those used in the MESSIDOR database. Two considerations can be made in relation to the results obtained by our method, both for the OD and fovea. On the one hand, they are consistent with the results obtained in the MESSIDOR database. On the other hand, our results are also competitive in relation to the non-simultaneous segmentation methods considered in the comparison. Therefore, from a global point of view, these results support and reinforce the hypothesis that our method is robust and independent of the database considered.

Also interesting is the approach presented in [62], where a deep learning framework is used for OD segmentation in fundus images. Although the Wang *et al*'s method does not segment the fovea, it shows how the simultaneous use of intra- and inter-SRK produces better segmentation results than when just intra-SRK is used. This result is in line with the methodology presented in our work. In particular, in [62], a Jaccard's index equal to 0.874 is obtained when only OD-intra-SRK is

Table 7: Comparison of our method with different competitive methods that address the OD segmentation problem using only intra-SRK. All the methods were evaluated using the 1200 MESSIDOR images. The standard deviation (SD) is also provided. The best results are highlighted in bold.

Method	**JC ± SD**	**D ± SD**	**Ac ± SD**	**TPF ± SD**	**FPF ± SD**
[Morales et al. 10]	0.8228 ± 0.1384	0.8950 ± 0.1056	0.9949 ± 0.0050	0.9300 ± 0.1239	0.0035 ± 0.0041
[Dashtbozorg et al. 18]	**0.8859 ± 0.0818**	**0.9373 ± 0.0509**	**0.9987 ± 0.0012**	**0.9481 ± 0.0459**	0.0008 ± 0.0010
[Rehman et al. 60]	0.747	0.851	0.988	0.948	0.012
This work	0.8730 ± 0.1254	0.9252 ± 0.1068	0.9985 ± 0.0020	0.9072 ± 0.1224	**0.0005 ± 0.0008**

Table 8: Comparison of our method with a competitive method that addresses the fovea segmentation problem using only intra-SRK. The best results are highlighted in bold.

Method	**Database**	#images	$\frac{1}{4}R_{OD}$	$\frac{1}{2}R_{OD}$	$1R_{OD}$
[GeethaRamani and Balasubramanian 61]	MESSIDOR	1200	85.0	94.1	**99.3**
This work	MESSIDOR	1200	**94.1**	**97.3**	99.0

used to train the model, but the mentioned index increases to 0.891 when vessel-intra-SRK, OD-intra-SRK and vessel-OD-inter-SRK are used simultaneously.

From the point of view of the output produced by the simultaneous segmentation method proposed in this work, Fig. 7 shows segmentation examples obtained for some MESSIDOR images. The method fails mainly in those images where there are severe signs of pathologies related to the macula (high number of micro-aneurysms or hemorrhages, or large hard exudates in the macular area) or the OD (advanced peripapillary atrophies or posterior staphylomas), such as is shown in Figs. 7.(e)-(f), respectively.

It should also be noted that the evolutionary search used in our method is separable from the proposed relational models. On the one hand, this means that the better each of the intra- and inter-structure models used is, the better the results should be in the evolutionary search for the OD and fovea. On the other hand, other DE variants or evolutionary algorithms could use the intra- and inter-structure models proposed here in order to try to improve our segmentation results.

Finally, the computation cost of the segmentation method is analyzed. The method was implemented with MATLAB language, in a laptop with CPU Intel Core i7-2640M, 2.8GHz and 8GB RAM. Table 11 shows a comparison of our approach with other methods in the literature that perform simultaneous segmentation of the OD and fovea. As these algorithms were implemented in a different computer system, the run-time should be interpreted in function of the hardware and programming language used. Although the results using convolutional neural networks (deep learning) are promising, the main drawbacks associated with these methods are the enormous amount of samples for training the model and the high computational cost to train and use the model. In particular, in [30], 4 538 439 pixels were used to train and test the model, each epoch of training took 9.83 hours (40 epochs of training and testing were run to create the neural network model), and a complete segmentation on a single image took 33.92 min (if the algorithm is run on GPUs, the segmentation can be completed in just under 10 min).

6 Conclusions

In this paper, we present a methodology for the simultaneous segmentation of anatomical structures in medical images. In particular, the methodology is instantiated in a method that is used to simultaneously segment the OD and fovea in retinal images. The idea is to build an OD-fovea model and use an evolutionary algorithm (differential evolution) to find the best model instance in a given retinal image that minimizes the error with respect to the model. The OD-fovea model integrates the intra-SRK of each structure with the inter-SRK of both and other structures.

The segmentation results obtained with our method are competitive compared with other recent methods in the literature, including methods that address segmentation individually, sequentially or simultaneously. Therefore, the proposed method shows that the joint use of relational models and evolutionary algorithms can be a useful tool for the recognition of patterns in medical images. A limitation of our method is given by the computational cost associated with the population-based solution search performed by the evolutionary algorithm. However, it is not difficult to parallelize an evolutionary algorithm if a computer cluster is available. In this case, the computational cost could be reduced considerably.

As future work, two main lines are open. On the one hand, other models could be proposed as intra- or intra&inter-SRK models and other evolutionary algo-

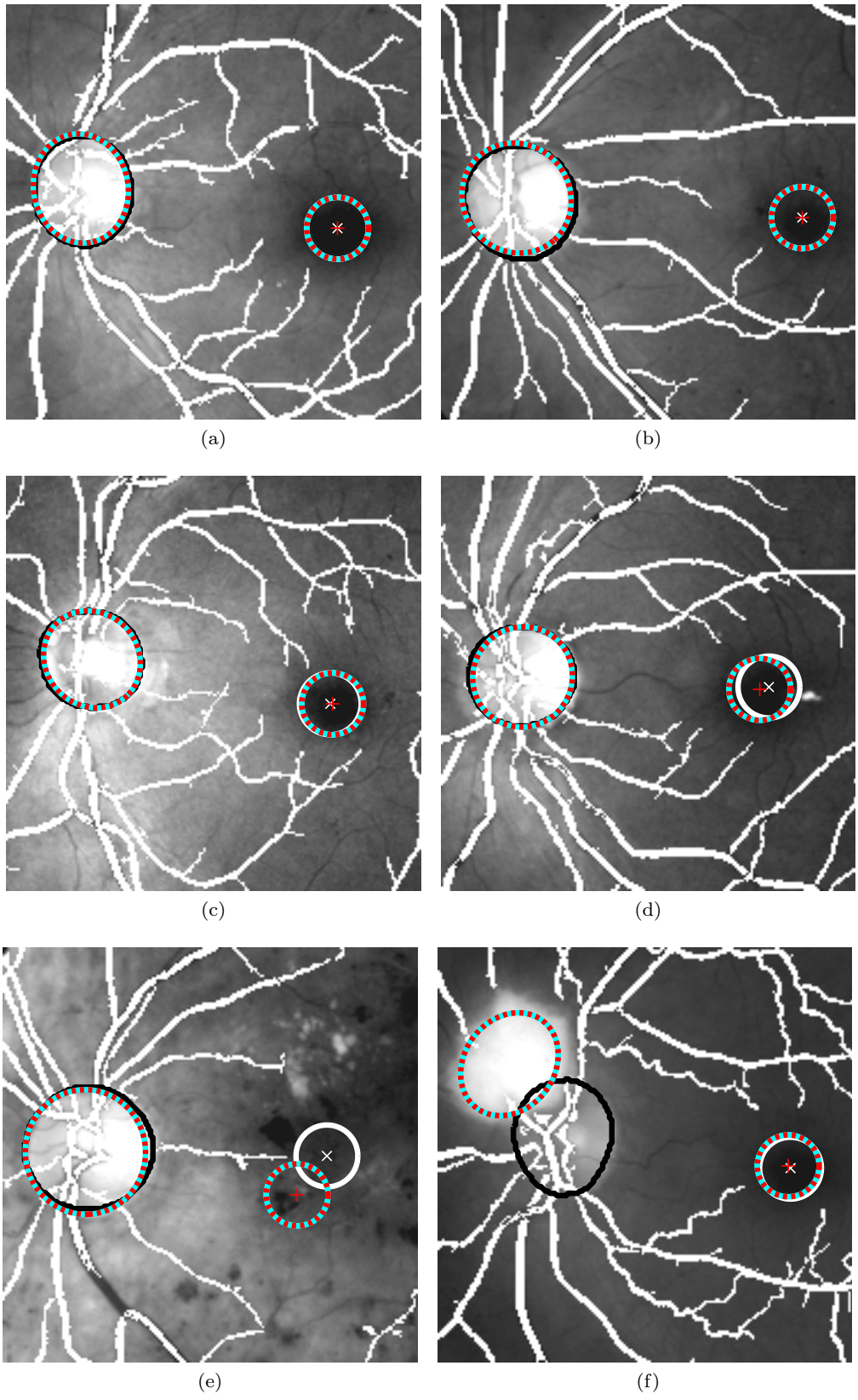

Fig. 7: Examples of segmentation obtained with our method for several MESSIDOR images: (a-b) both structures are segmented with a very good approximation; (c-d) both structures are segmented with a good approximation; (e) just the OD is correctly segmented; (f) just the fovea is correctly segmented. The solid line represents the gold standard and, the dashed line, the segmentation obtained. See color figure online.

Table 9: Comparison of our method with other competitive methods that address the OD segmentation problem in the ONHSD database. The standard deviation (SD) is also provided. The best results are highlighted in bold.

Method	**JC ± SD**	**D ± SD**	**Ac ± SD**	**TPF ± SD**	**FPF ± SD**
[Girard et al. 29] [1]	0.8400	-	-	-	-
[Morales et al. 10]	0.8045 ± 0.1175	0.8867 ± 0.0776	0.9941 ± 0.0042	0.9310 ± 0.1046	0.0043 ± 0.0042
[Dashtbozorg et al. 18]	0.8341± 0.0912	**0.9173± 0.0634**	0.9968± 0.0027	**0.9435± 0.0791**	0.0012± 0.0027
[Rehman et al. 60]	0.824	0.897	0.993	0.924	0.005
This work	**0.8417± 0.1132**	0.9083± 0.0971	**0.9979± 0.0022**	0.8756 ± 0.1153	**0.0005± 0.0010**

[1] This work uses OD and fovea simultaneous segmentation but it does not provides results for the fovea in the ONHSD database.

Table 10: Success rate comparison (in %) of our method with other competitive methods that address the fovea segmentation problem in the DIARETDB1 database. The best results are highlighted in bold.

Method	**Database**	#images	$\frac{1}{4}R_{OD}$	$\frac{1}{2}R_{OD}$	$1R_{OD}$	$2R_{OD}$
[Welfer et al. 5]	DIATETDB1	89	-	-	92.1	-
[Qureshi et al. 63]	DIATETDB1	89	-	-	98.7	-
[Medhi and Dandapat 6]	DIATETDB1	89	-	-	95.5	-
[Kao et al 26]	DIATETDB1	89	-	-	92.1	94.4
[Aquino 27]	DIATETDB1	89	44.9	70.8	94.4	**100**
[GeethaRamani and Balasubramanian 61]	DIATETDB1	89	51.7	88.8	97.7	**100**
This work	DIARETDB1	89	**79.4**	**93.1**	**100**	**100**

Table 11: Comparison of OD and fovea simultaneous segmentation methods, considering the hardware, programming language and computation time used.

Method	**Hardware**	**Language**	**Time (s)**
[Girard et al. 29]	Multi-core processing	C++	6.4
[Tan et al. 30]	Two Intel Xeon, 2.66GHz, 24GB RAM	MATLAB	2035
This work	Intel Core i7-2640M, 2.8GHz, 8GB RAM	MATLAB	29.35 ± 0.91

rithms (or metaheuristic in general) could be used as an optimization method to tune the relational model parameters. On the other hand, the proposed methodology could be used for segmentation of anatomical structures in other types of medical images.

Acknowledgments

The authors would like to thank the ONHSD and MESSIDOR program partners for facilitating their respective databases. We would also like to express our gratitude to Gegundez-Arias *et al.* [25] for allowing us to access their MESSIDOR fovea ground truth.

Compliance with ethical standards

Conflict of interest: The authors declare that they have no conflict of interest.

References

1. L.D. Hubbard, R.J. Brothers, W.N. King, L.X. Clegg, R. Klein, L.S. Cooper, A.R. Sharrett, M.D. Davis, and J. Cai. Methods for evaluation of retinal microvascular abnormalities associated with hypertension/sclerosis in the atherosclerosis risk in communities study. *Ophthalmology*, 106(12):2269–2280, 1999.
2. Niall Patton, Tariq M. Aslam, Thomas MacGillivray, Ian J. Deary, Baljean Dhillon, Robert H. Eikelboom, Kanagasingam Yogesan, and Ian J. Constable. Retinal image analysis: Concepts, applications and potential. *Progress in Retinal and Eye Research*, 25(1):99–127, 2006.
3. Aliaa Abdel-Haleim Abdel-Razik Youssif, Atef Zaki Ghalwash, and Amr Ahmed Sabry Abdel-Rahman Ghoneim. Optic disc detection from normalized digital fundus images by means of a vessels' direction matched filter. *IEEE Transaction on Medical Imaging*, 27(1):11–18, 2008.
4. R.J. Winder, P.J. Morrow, I.N. McRitchie, J.R. Bailie, and P.M. Hart. Algorithms for digital image processing in diabetic retinopathy. *Computerized Medical Imaging and Graphics*, 33(8):608–622, 2009.
5. D. Welfer, J. Scharcanski, and D.R. Marinho. Fovea center detection based on the retina anatomy and mathematical morphology. *Comput. Meth. Prog. Bio.*, 104(3):397–409, 2011.

6. J.P. Medhi and S. Dandapat. An effective fovea detection and automatic assessment of diabetic maculopathy in color fundus images. *Comput. Biol. Med.*, 74:30 – 44, 2016.
7. J. M. Molina-Casado, E. J. Carmona, and J. García-Feijoó. Fast detection of the main anatomical structures in digital retinal images based on intra- and inter-structure relational knowledge. *Computer Methods and Programs in Biomedicine*, 149:55–68, 2017.
8. A. Aquino, M. E. Gegúndez-Arias, and D. Marin. Detecting the optic disc boundary in digital fundus images using morphological, edge detection, and feature extraction techniques. *IEEE Transactions on Medical Imaging*, 29(11):1860–1869, 2010.
9. D. Welfer, J. Scharcanski, C. M. Kitamura, M. M. Dal Pizzol, L. W. B. Ludwig, and R. D. Marinho. Segmentation of the optic disk in color eye fundus images using an adaptive morphological approach. *Computers in Biology and Medicine*, 40(2):124–137, 2010.
10. S. Morales, V. Naranjo, J. Angulo, and M. L. Alcañiz. Automatic detection of optic disc based on PCA and mathematical morphology. *IEEE Transactions on Medical Imaging*, 32(4):786–796, 2013.
11. X. Zhu, R. M. Rangayyan, and A. L. Ells. Detection of the optic nerve head in fundus images of the retina using the hough transform for circles. *Journal of Digital Imaging*, 23(3):332–341, 2010.
12. E. J. Carmona, M. Rincón, J. García-Feijoo, and J. M. Martínez-de-la Casa. Identification of the optic nerve head with genetic algorithms. *Artificial Intelligence in Medicine*, 43:243–259, 2008.
13. J. Novo, M. G. Penedo, and J. Santos. Localisation of the optic disc by means of GA-optimised topological active nets. *Image and Vision Computing*, 27(10):1572–1584, 2009.
14. J. M. Molina and E. J. Carmona. Localization and segmentation of the optic nerve head in eye fundus images using pyramid representation and genetic algorithms. In J.M. Ferrández et al, editor, *Foundations on Natural and Artificial Computation (Part I)*, pages 431–440. Springer, 2011.
15. Rafael Arnay, Francisco Fumero, and Jose Sigut. Ant colony optimization-based method for optic cup segmentation in retinal images. *Applied Soft Computing*, 52:409 – 417, 2017.
16. J. Lowell, A. Hunter, D. Steel, A. Basu, R. Ryder, and E. Fletcher. Optic nerve head segmentation. *IEEE Transactions on medical Imaging*, 23(2):256–264, 2004.
17. A. Giachetti, L. Ballerini, and E. Trucco. Accurate and reliable segmentation of the optic disc in digital fundus images. *Journal of Medical Imaging*, 1(2):024001–024001, 2014.
18. B. Dashtbozorg, A. M. Mendonça, and A. Campilho. Optic disc segmentation using the sliding band filter. *Computers in Biology and Medicine*, 56:1–12, 2015.
19. H. Yu, E. S. Barriga, C. Agurto, S. Echegaray, M. S. Pattichis, W. Bauman, and P. Soliz. Fast localization and segmentation of optic disk in retinal images using directional matched filtering and level sets. *IEEE Transactions on Information Technology in Biomedicine*, 16(4):644–657, 2012.
20. J. Cheng, J. Liu, Y. Xu, F. Yin, D. W. K. Wong, N.-M. Tan, D. Tao, C.-Y Cheng, T. Aung, and T. Y. Wong. Superpixel classification based optic disc and optic cup segmentation for glaucoma screening. *IEEE Transactions on Medical Imaging*, 32(6):1019–1032, 2013.
21. J. Singh, G. D. Joshi, and J. Sivaswamy. Appearance-based object detection in colour retinal images. In *15th IEEE International Conference on Image Processing*, pages 1432–1435. IEEE, 2008.
22. A. Salazar-Gonzalez, D. Kaba, Y. Li, and X. Liu. Segmentation of the blood vessels and optic disk in retinal images. *IEEE Journal of Biomedical and Health Informatics*, 18(6):1874–1886, 2014.
23. D. Marin, M.E. Gegundez-Arias, A. Suero, and J.M. Bravo. Obtaining optic disc center and pixel region by automatic thresholding methods on morphologically processed fundus images. *Comput. Meth. Prog. Bio.*, 118(2):173 – 185, 2015.
24. H. Yu, E. S. Barriga, C. Agurto, S. Echegaray, M. Pattichis, G. Zamora, W. Bauman, and P. Soliz. Fast localization of optic disc and fovea in retinal images for eye disease screening. In *SPIE Medical Imaging*, volume 7963, pages 796317–796329, 2011.
25. M. E. Gegundez, D. Marin, J. M. Bravo, and A. Suero. Locating the fovea center position in digital fundus images using thresholding and feature extraction techniques. *Computerized Medical Imaging and Graphics*, 37(5):386–393, 2013.
26. E. F. Kao, P.-C. Lin, M.-C. Chou, T. S. Jaw, and G. C. Liu. Automated detection of fovea in fundus images based on vessel-free zone and adaptive gaussian template. *Computer Methods and Programs in Biomedicine*, 117(2):92–103, 2014.
27. A. Aquino. Establishing the macular grading grid by means of fovea centre detection using anatomical-based and visual-based features. *Computers in Biology and Medicine*, 55:61–73, 2014.
28. K. S. Chin, E. Trucco, L. Tan, and P. J. Wilson. Automatic fovea location in retinal images using anatomical priors and vessel density. *Pattern*

Recognition Letters, 34(10):1152–1158, 2013.

29. F. Girard, C. Kavalec, S. Grenier, H. B. Tahar, and F. Cheriet. Simultaneous macula detection and optic disc boundary segmentation in retinal fundus images. In *SPIE Medical Imaging*, volume 9784, pages 97841F1–97841F9, 2016.
30. J. H. Tan, U. R. Acharya, S. V. Bhandary, K. C. Chua, and S. Sivaprasad. Segmentation of optic disc, fovea and retinal vasculature using a single convolutional neural network. *Journal of Computational Science*, 20:70–79, 2017.
31. MESSIDOR. Messidor database. `http://www.adcis.net/en/third-party/messidor/`, 2012. (last access 2019/03/22).
32. E. Decenciere, X. Zhang, G. Cazuguel, B. Lay, B. Cochener, C. Trone, P. Gain, R. Ordonez, P. Massin, A. Erginay, B. Charton, and J. C. Klein. Feedback on a publicly distributed database: the messidor database. *Image Analysis & Stereology*, 33(3):231–234, 2014.
33. ONHSD. Optic nerve head segmentation dataset. `http://www.aldiri.info/Image%20Datasets/ONHSD.aspx`, 2013. (accessed 2019/03/22).
34. DIARETDB1. The diabetic retinopathy database. `http://www.it.lut.fi/project/imageret/diaretdb1/`, 2015. (accessed 2019/03/22).
35. T. Kauppi, V. Kalesnykiene, J.K. Kamarainen, L. Lensu, I. Sorri, A. Raninen, R. Voutilainen, H. Uusitalo, H. Kälviäinen, and J. Pietilä. The diaretdb1 diabetic retinopathy database and evaluation protocol. In *Proceedings of the 11th Conf. on Medical Image Understanding and Analysis*, pages 61–65, 2007.
36. UniHuelva. Messidor fovea annotations. `http://www.uhu.es/retinopathy/muestras/Provided_Information.zip`, 2013. (last access 2019/03/22).
37. A. Atkinson and C. Mazo. Imaged area of the retina. `https://www.freelists.org/archives/optimal/02-2017/pdf91WmMGLh6Q.pdf`, 2011. (last access 2019/03/22).
38. S. Lee, M. D. Abramoff, and J. M. Reinhardt. Retinal atlas statistics from color fundus images. In *SPIE Medical Imaging*, volume 7623, pages 762310–762319, 2010.
39. P. M. D. S. Pallawala, W. Hsu, M. L. Lee, and K-G A. Eong. Automated optic disc localization and contour detection using ellipse fitting and wavelet transform. In Tomás Pajdla and Jiří Matas, editors, *8th European Conference on Computer Vision*, pages 139–151, Berlin, Heidelberg, 2004. Springer.
40. J. Cheng, J. Liu, D. W. K. Wong, F. Yin, C. Cheung, M. Baskaran, T. Aung, and T. Y. Wong. Automatic optic disc segmentation with peripapillary atrophy elimination. In *Annual International Conference of the IEEE Engineering in Medicine and Biology Society*, pages 6224–6227. IEEE, 2011.
41. S. Roychowdhury, D. D. Koozekanani, S. N. Kuchinka, and K. K. Parhi. Optic disc boundary and vessel origin segmentation of fundus images. *IEEE Journal of Biomedical and Health Informatics*, 20(6):1562–1574, Nov 2016.
42. J. B. Raja and C. G. Ravichandran. Automatic localization of fovea in retinal images based on mathematical morphology and anatomic structures. *International Journal of Engineering & Technology*, 6(5):2171–2183, 2014.
43. J. Schwiegerling. *Field guide to visual and ophthalmic optics*. Bellingham, WA:SPIE Press, 2004.
44. X. Xu. Simultaneous automatic detection of optic disc and fovea. Master's thesis, University of Iowa, 2010.
45. C. Sinthanayothin, J. F. Boyce, H. L. Cook, and T. H. Williamson. Automated localisation of the optic disc, fovea, and retinal blood vessels from digital colour fundus images. *British Journal of Ophthalmology*, 83(8):902–910, 1999.
46. R. A. Jonas, Y. X. Wang, H. Yang, J. J. Li, L. Xu, S. Panda-Jonas, and J. B. Jonas. Optic disc - fovea angle: The beijing eye study 2011. *PLOS ONE*, 10(11):1–10, 11 2015.
47. R. Storn and K. Price. Differential evolution - a simple and efficient heuristic for global optimization over continuous spaces. *Journal of Global Optimization*, 11(4):341–359, 1997.
48. S. Das and P. N. Suganthan. Differential evolution: A survey of the state-of-the-art. *IEEE Transactions on Evolutionary Computation*, 15(1):4–31, 2011.
49. Roberto Ugolotti, Youssef S.G. Nashed, Pablo Mesejo, Spela Ivekovic, Luca Mussi, and Stefano Cagnoni. Particle swarm optimization and differential evolution for model-based object detection. *Applied Soft Computing*, 13(6):3092–3105, 2013.
50. P. Mesejo, R. Ugolotti, F. Di Cunto, M. Giacobini, and S. Cagnoni. Automatic hippocampus localization in histological images using differential evolution-based deformable models. *Pattern Recognition Letters*, 34(3):299–307, 2013.
51. M. Saraswat, K. V. Arya, and H. Sharma. Leukocyte segmentation in tissue images using differential evolution algorithm. *Swarm and Evolutionary Computation*, 11:46–54, 2013.
52. Pablo Mesejo, Óscar Ibañez, Óscar Cordón, and Stefano Cagnoni. A survey on image segmenta-

tion using metaheuristic-based deformable models: state of the art and critical analysis. *Applied Soft Computing*, 44:1–29, 2016.
53. John H. Holland. *Adaptation in Natural and Artificial Systems: An Introductory Analysis with Applications to Biology, Control and Artificial Intelligence*. MIT Press, Cambridge, MA, USA, 1992.
54. Hans-Georg Beyer and Hans-Paul Schwefel. Evolution strategies – A comprehensive introduction. *Natural Computing*, 1:3–52, 2002.
55. N. Hansen and A. Ostermeier. Completely derandomized self-adaptation in evolution strategies. *Evolutionary Computation*, 9(2):159–195, 2001.
56. James Kennedy and Russell C. Eberhart. *Swarm Intelligence*. Morgan Kaufmann Publishers Inc., San Francisco, CA, USA, 2001.
57. Shuihua Wang, Yudong Zhang, Genlin Ji, Jiquan Yang, Jianguo Wu, and Ling Wei. Fruit classification by wavelet-entropy and feedforward neural network trained by fitness-scaled chaotic abc and biogeography-based optimization. *Entropy*, 17:5711–5728, 2015.
58. Shuihua Wang, Peng Li, Peng Chen, Preetha Phillips, Ge Liu, Sidan Du, and Yudong Zhang. Pathological brain detection via wavelet packet tsallis entropy and real-coded biogeography-based optimization. *Fundamenta Informaticae*, 151:275–291, 2017.
59. K. Price, R. M. Storn, and J. A. Lampinen. *Differential Evolution: A Practical Approach to Global Optimization (Natural Computing Series)*. Springer-Verlag New York, Inc., Secaucus, NJ, USA, 2005.
60. Zaka Ur Rehman, Syed S. Naqvi, Tariq M. Khan, Muhammad Arsalan, Muhammad A. Khan, and M.A. Khalil. Multi-parametric optic disc segmentation using superpixel based feature classification. *Expert Systems with Applications*, 120:461–473, 2019.
61. R. GeethaRamani and L. Balasubramanian. Macula segmentation and fovea localization employing image processing and heuristic based clustering for automated retinal screening. *Computer Methods and Programs in Biomedicine*, 160:153–163, 2018.
62. Lei Wang, Han Liu, Yaling Lu, Hang Chen, Jian Zhang, and Jiantao Pu. A coarse-to-fine deep learning framework for optic disc segmentation in fundus images. *Biomedical Signal Processing and Control*, 51:82–89, 2019.
63. Rashid Jalal Qureshi, Laszlo Kovacs, Balazs Harangi, Brigitta Nagy, Tunde Peto, and Andras Hajdu. Combining algorithms for automatic detection of optic disc and macula in fundus images. *Computer Vision and Image Understanding*, 116(1):138–145, 2012.